BULLETIN OF THE EARTHQUAKE
RESEARCH INSTITUTE
UNIVERSITY OF TOKYO
Vol. 61 (1986) pp. 97-127

Strong Ground Motion Simulation of the 1976 Ninghe, China Earthquake

Yifan YUAN*, Shizuyo YOSHIZAWA and Yutaka OSAWA
Earthquake Research Institute
(Received January 31, 1986)

Abstract

The strong ground motions observed during the Nov. 15, 1976 Ninghe, China earthquake (M=6.9) have been simulated by the finite difference method. By analyzing observed accelerograms, an acceleration source function of impulsive shape is assumed for synthesizing observed accelerograms. The effects of lateral heterogeneity of ground structures are taken into account in this study. The simulated results show that the energy was released in a small region surrounding the hypocenter in the Ninghe earthquake, the strike slip was predominant on the fault and the maximum acceleration might be over 1 g at the hypocenter. Even with a relatively simple rupture process, ground motions become complicated due to reflection and scattering of seismic waves, especially in laterally heterogeneous ground structure.

1. Introduction

In order to prevent and mitigate earthquake disasters, it is necessary to assess hazards caused by future earthquakes. An estimation of strong ground motions is important for the hazard assessment. Great efforts have been made for investigating strong ground motions in recent years. The time histories of ground displacement or/and velocity have successfully been simulated for some particular earthquakes by assuming simple models of source mechanisms and ground structures (AKI, 1968; HASKELL, 1969; MIKUMO, 1973; TRIFUNAC, 1974; HEATON *et al.*, 1979; BOUCHON, 1982; OLSON *et al.*, 1982; IMAKAWA *et al.*, 1984; ARCHULETA, 1984). These results were limited, however, to long period components of ground motions (say, greater than one second). Recent studies have shown that it is possible to analyze near-field seismic ground motions in a short period range considering a more complex rupture process on the fault, such as barrier or asperity model (AKI, 1982; BOORE, 1983). On the other hand, the short period strong ground motions that may produce major damage to ordinary structures is considered as having resulted from multi-

* On leave from Institute of Engineering Mechanics, China.

reflection of seismic waves in shallow sediment layers or scattering waves propagating in the heterogeneous ground. If the wavelength investigated is in the range of the same order as the characteristic dimension of the heterogeneous structure, such as the radius of sediment basin, the effects of heterogeneity should be taken into account (WONG *et al.*, 1977). It brings on, however, much more difficulty in analyses, so that only a few cases can be solved analytically. Numerical methods have been successfully used for calculating near-field seismograms and other dynamic problems, especially when the wave fields in the vicinity of heterogeneous ground structures or sources are taken under consideration (BOORE, 1972; ALTERMAN *et al.*, 1972; LIAO *et al.*, 1980; FUYUKI *et al.*, 1980; ZAMA, 1981; YUAN *et al.*, 1984).

Seismic ground motions may depend on complex dynamic rupture processes on the fault, crustal and recording site ground structures. In order to study their effects on seismic ground motions, an effective approach was introduced by investigating observed seismograms at a particular region, where the crustal and ground structures are well known. Therefore the effects of source, crust and site may be estimated individually. In most cases, however, the site conditions, crustal structure and earthquake rupture process are not well known and effects of these factors are not well separated. In this study, particular characteristics of the strong ground motions observed for the 1976 Ninghe earthquake are used to constrain fault parameters in advance. Moreover, the lateral inhomogeneity of underground structure at observation stations is taken into account in the simulation to interpret the complexity of strong seismic ground motions.

At first, the time histories of ground acceleration observed during the Ninghe earthquake were investigated. Based on the investigation, we propose an acceleration source function of impulsive shape to describe faulting process at the source. According to the available data, three ground models were constructed for different observation stations. A vertical interface was introduced to study the effects of lateral heterogeneity of observation sites. Then synthetic accelerograms were computed by the finite difference method. The unified transmitting method was used to deal with transmitting boundaries in numerical calculation. With explanation about the computational models, we present some measures for saving the memory storage and CPU time of computers. In the last part we describe what parameters affect synthetic accelerograms sensitively and compare synthetic accelerograms and their response spectra with observed ones. Meanwhile the character of the Ninghe earthquake is discussed briefly.

2. Description of the Earthquake

The Ninghe earthquake was the second strongest aftershock of the Tangshan, China earthquake. The Tangshan earthquake brought about a great loss of life and caused extensive damage. Fig. 1 shows a map of the Beijing-Tianjin-Tangshan area with earthquake epicenters and the locations of accelerographs. Cross 1 shows the epicenter of the main shock of the Tangshan earthquake, crosses 2 and 3 show the strongest aftershocks. Cross 3 shows the epicenter of the Ninghe earthquake of magnitude $M=6.9$, which occured on Nov. 15, 1976 at a depth of 15 km. These parameters are shown in Table 1. Fig. 2 illustrates data on P-wave first-motions and a possible fault plane solution of the earthquake (ZHANG *et al.*, 1980; ZHAO *et al.*, 1984). The distribution of aftershocks,

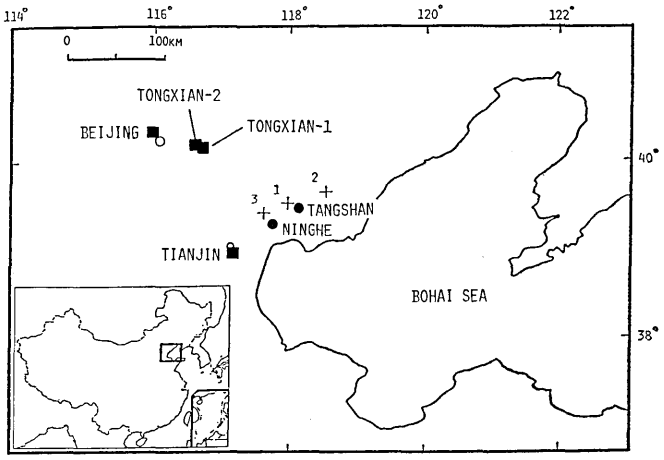

Fig. 1. Map view of the Beijing-Tianjin-Tangshan area showing epicenters of Tanshan earthquakes (the main shock and the two strongest aftershocks) by crosses and locations of accelerographs used in this study by squares. Outline of China within the frame shows the approximate location of this area.

Table 1. Parameters of the Tangshan earthquakes. The number of each earthquake is shown in Fig. 1.

No.	Occurence Date	Origin time	Latitude	Longitude	Depth (km)	Magnitude
1	July 27, 1976	19h 42m UT	39°36′N	118°00′E	22	7.8
2	July 28, 1976	10h 45m UT	39°40′N	118°34′E	23	7.1
3	Nov. 15, 1976	13h 53m UT	39°24′N	117°38′E	15	6.9

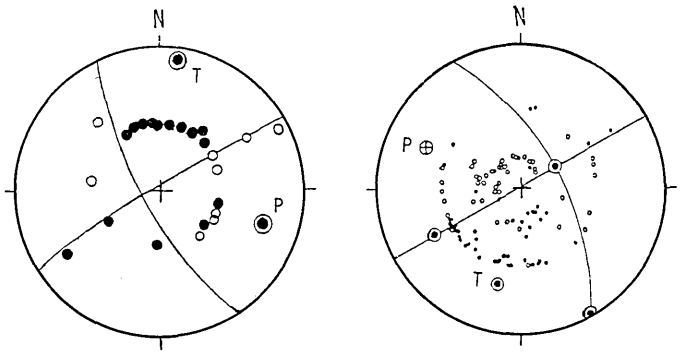

Fig. 2. The first P motions and fault plane solution of the Ninghe earthquake. The solid and empty circles indicate local (on the left, ZHAO *et al.*, 1984) and global (on the right, from ZHANG *et al.*, 1980) compressional and dilatational projects, respectively. According to analyses of rupture mechanism and distribution of aftershocks, the plane of strike N30°W is determined as the fault plane of the Ninghe earthquake.

Table 2. Fault plane solution of the Nov. 15, 1976 Ninghe earthquake.

Plane 1		Plane 2		P-axis		T-axis	
Strike	Dip angle	Strike	Dip angle	Direction	Dip angle	Direction	Dip angle
*60 SE	80	149 NE	70	105	20	10	20
**60 SE	90	150 NE	60	289	21	191	21

* from ZHAO *et al.*, 1984.
** from ZHANG *et al.*, 1980.

whose magnitudes were greater than 5.0 and occurred after the main shock is shown in Fig. 3a (ZHANG *et al.*, 1980). The distribution of aftershocks occurred in one day after the Ninghe earthquake, while some aftershocks of the main shock are also shown in Fig. 3b (ISHIKAWA *et al.*, 1983). The aftershocks of the Ninghe earthquake seem to be distributed along a line in a NNW direction which is nearly perpendicular to the line of aftershock distribution of the main shock, and they are located in a narrow band within a segment of about 20 km. Because there is no trace of faults on the ground surface in the Ninghe region, we will assume that the fault of the Ninghe earthquake runs N30°W according to the aftershock distribution. The length and width of the fault are assumed to be 20 km and 12.5 km, respectively. As will be explained later, the length and width of the fault are not significant for simulating ground motions of the Ninghe earthquake. Since the dip

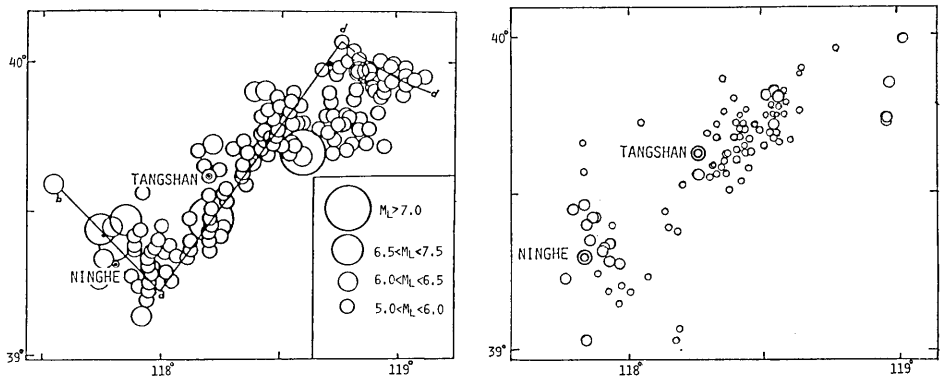

Fig. 3. The aftershock distribution of the Tangshan earthquake for magnitudes greater than 5.0 until Aug., 1978, is shown in Fig. 3a. Aftershocks of the main shock are distributed along direction NNE while aftershocks of the two strongest aftershocks seem to be distributed on the line perpendicular to that line. In Fig. 3b, large circles show aftershocks during the one day after the Ninghe earthquake, while small circles show aftershocks of the main shock with magnitudes greater than 2.0.

angle of the fault is greater than 60° or 70° (Table 2), we assume the fault is vertical for simplification. With these assumptions a satisfactory simulation of strong ground motion was obtained for the Ninghe earthquake as shown in the following.

3. Strong Ground Motion Records

Accelerograms of the Ninghe earthquake were recorded at several observation stations in northern China. The accelerograms recorded at the four stations shown in Fig. 1 are suitable for study. The four stations are: Tianjin (Δ=52 km), Beijing (Δ=128 km), Tongxian-1 (Δ=99 km) and Tongxian-2 (Δ=102 km). The Tongxian-1 and Tongxian-2 are near each other.

Fig. 4 illustrates the accelerograms at the four stations, among which the maximum acceleration of 146 gal was recorded in the NS component of Tianjin records. These observed records suggest the following features.

(1) There is a noticeable pulse-shaped waveform in all the horizontal components of observed accelerograms, particularly in the Tianjin records, in which large pulse waveforms arrived at the same time in the two horizontal components. LIN *et al.* (1979) have corrected the location of the epicenter taking this pulse wave as the arrival of the first *S*-wave in their study. The redetermined epicenter is closer to the region with the most serious damage than that determined by the seismograph net-

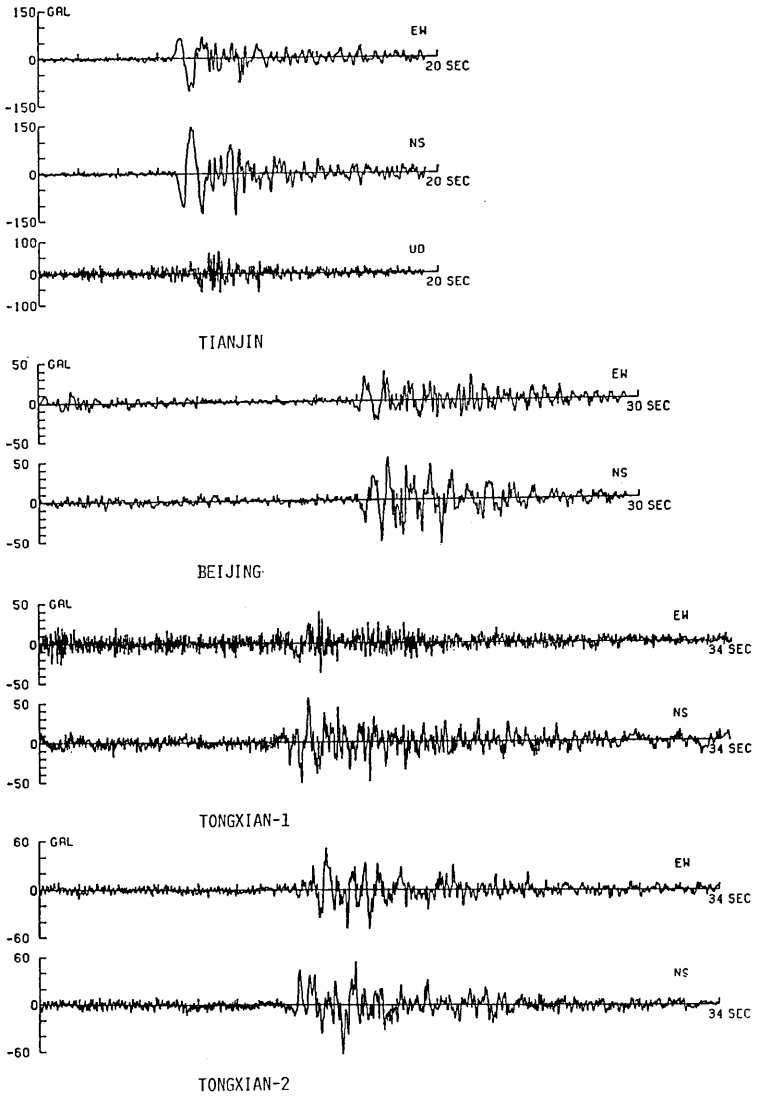

Fig. 4. Accelerograms of the Ninghe earthquake (Nov. 15, 1976, M=6.9) recorded at Tianjin, Beijing and Tongxian (see Fig. 1) with the maximum acceleration of 146 gal at the NS component the Tianjin records. There are two stations in Tongxian (1 and 2). It is noticeable that a relatively long period wave (period about 1 second) is predominant in all of the accelerograms recorded at the different stations.

work located in northern China. We adopt this assumption that the large pulse waveforms are the first direct S-waves in the following analyses. In fact, if we assume the source function has an impulsive shape, the seismic waves radiated by the source will also have an impul-

sive shape (YUAN *et al.*, 1984). According to this property, we assume an acceleration source function of an impulsive shape (Fig. 10) for synthesizing accelerograms.

(2) All of these accelerograms contain a relatively long period wave, although these stations are located in different places. From Fig. 5, which shows the Fourier spectra of these records, we can conclude with confidence that a predominant component of a period of about 1 second exists in all of these records.

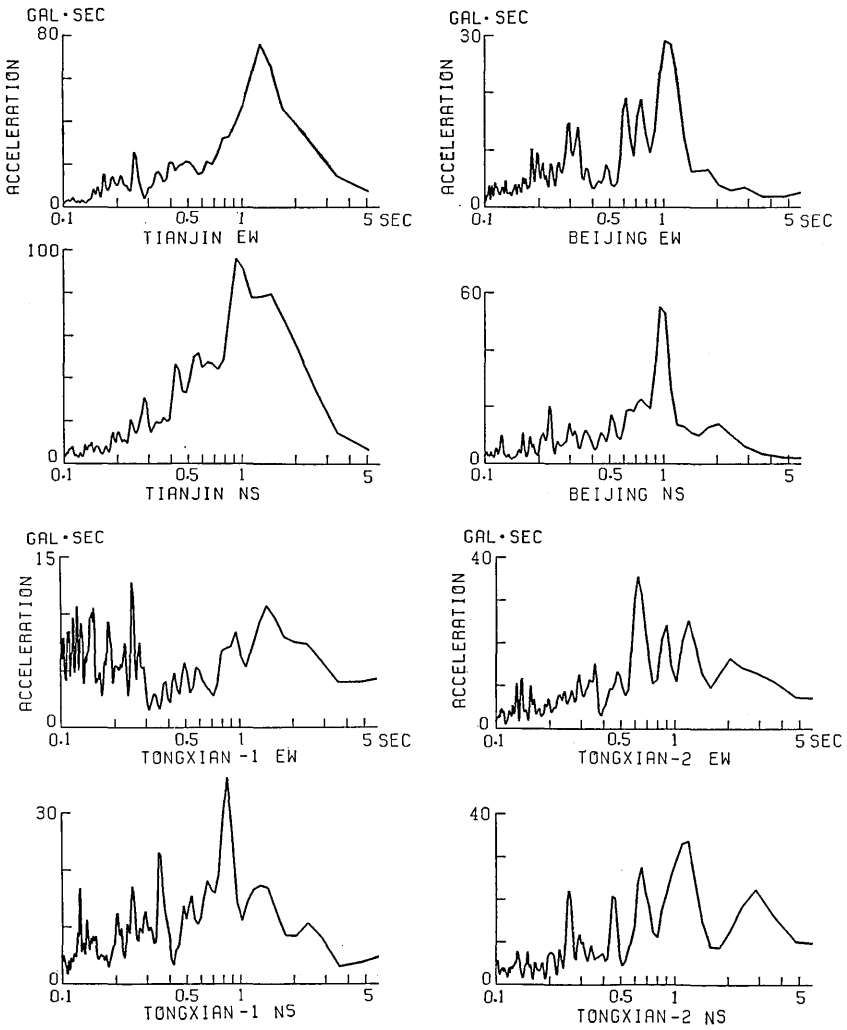

Fig. 5. The Fourier spectra of observed acceleration records during the Ninghe earthquake. The component of a period of about 1 sec is predominant in all of these spectra.

In fact, in accelerograms observed in Tianjin during the other earthquakes, which also occured in northern China, any component of period about 1 second is not predominant (PENG, personal communication, 1985). It may prove that the component does not reflect the local site property, in other words, it may come from the source mechanism of this particular earthquake. According to this assumption, we assume the duration of the acceleration impulse is 1 second in the source function (Fig. 10). That is, the source radiates the wave of a period of about 1 second predominately.

(3) The difference of epicentral distance between the stations Tongxian-1 and Tongxian-2 is only about 3 km, but their time histories of ground acceleration are fairly different from each other. A horizontal layer model can not explain this phenomenon, because there is no obvious difference between ground acceleration waveforms when seismic waves propagate in a horizontal layer model (Fig. 16, Fig. 17). A reasonable explanation is that it may have resulted from lateral heterogeneity of ground structures between the two stations.

Since the EW component of records in Tongxian-1 is very small having abundant high frequency components as compared with the NS one, the accelerograph may have been involved with some trouble.

(4) Another interesting aspect appears in their acceleration response spectra (Fig. 6). For example, in the spectrum of the NS component of Tianjin, if the damping factor is changed, peak values at the period of about 1 second do not change so significantly as the other peak values, say, at the period of about 0.3 second. It might be explained as follows: the response of a single freedom system being applied by an impulse will be different from the case of succesive impulses. Obviously, if damping of the system is changed, the response of the former will not change so remarkably as that of the latter. Similarly, in the spectrum mentioned above, the peak values at about 0.3 second might be caused by succesive impulses, which are produced by multi-reflecting waves in sediment layers. Therefore, the peak values may reflect the property of the ground structure. In contrast, the peak values at about 1 second might be caused by an impulsive wave which came from the source directly.

(5) The vertical components were not recorded except at Tianjin. We can not use, then, vertical components as a measure checking the validity of our simulation.

For the purpose of comparing more clearly between the observed and the synthetic accelerograms we filtered the observed records using a low-pass filter with the cut-off frequency of 2 Hz (Fig. 7). Comparing Fig. 7 with Fig. 4, one can find that the filtered accelerograms keep the

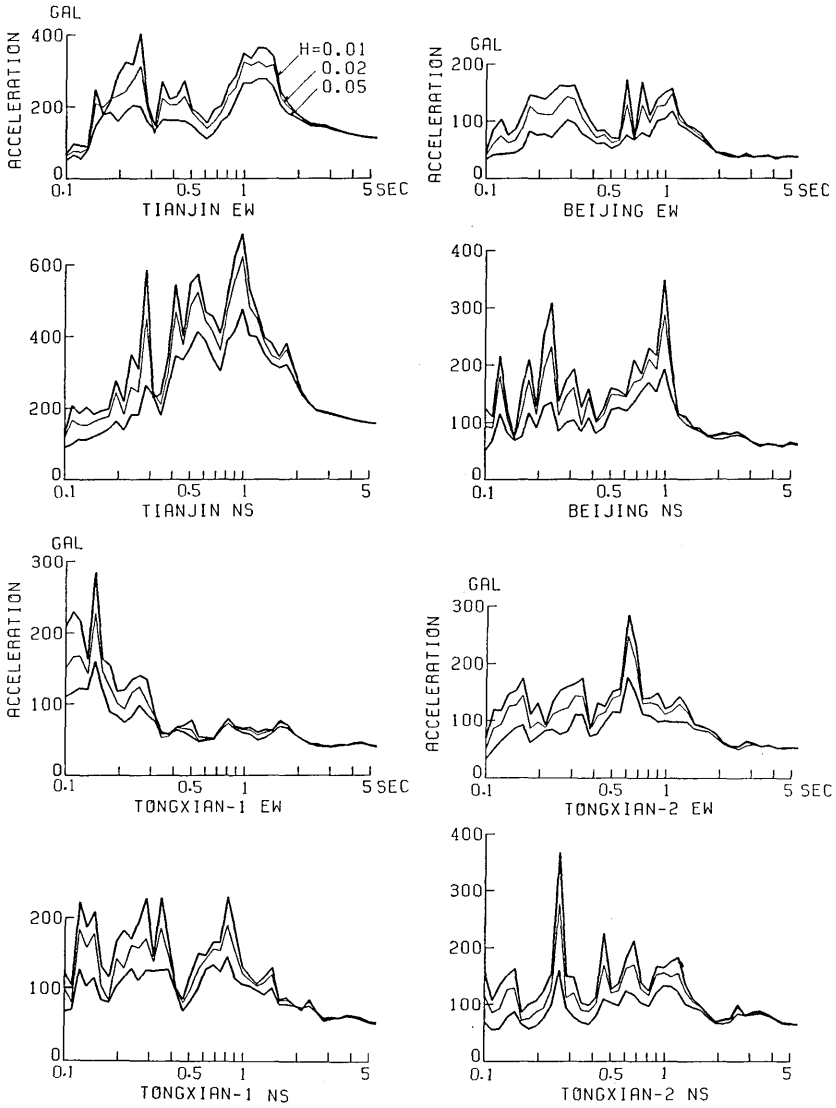

Fig. 6. The acceleration response spectra of observed records during the Ninghe earthquake. H is damping factor.

principal features of the original ones. The large pulse-shaped waveforms appear in all the accelerograms, thus indicating they may be produced at the source.

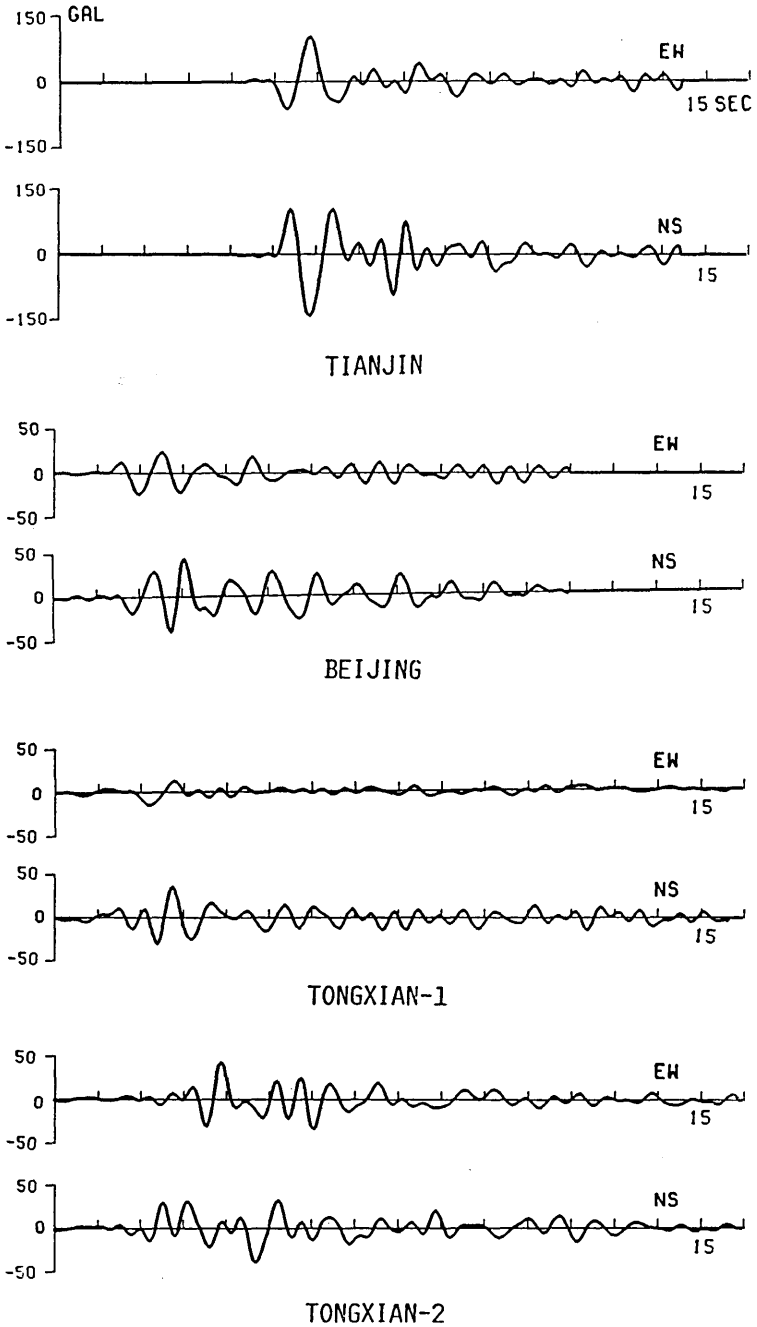

Fig. 7. Filtered accelerograms of the Ninghe earthquake by a low-pass filter with cut-off frequency of 2 Hz. Principal features of the observed records are retained.

4. Faulting Model

The representation theory of dislocation (MARUYAMA, 1963) is used to synthesize theoretical accelerograms. The source fault model drawn in the Cartesian coodinates with the origin located at the source point is shown in Fig. 8. ν is the normal unit vector of the fault plane. θ

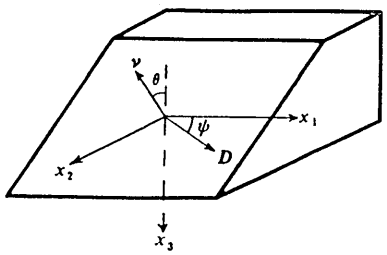

Fig. 8. The source coodinate system. D is the dislocation vector on the fault. ν is the normal vector of the fault plane. θ is equal to the dip angle of the fault. ψ is the angle between the dislocation vector and the axis X_1.

is equal to the dip angle of the fault, D is the dislocation vector and $D=D_0F(t)$, where D_0 is the peak value and $F(t)$ is the source time function. ψ is the angle between the dislocation vector and the axis X_1. The original representation formula may be rewritten, after some deduction and rearrangement, in the cylindrical coodinates (r, φ, z) as follows:

$$\begin{aligned} \boldsymbol{u}_s = {} & \boldsymbol{u}_s^{\mathrm{I}}(r, \varphi, z) \sin\psi \cos 2\theta + \boldsymbol{u}_s^{\mathrm{II}}\left(r, \varphi - \frac{\pi}{2}, z\right) \cos\psi \cos 2\theta \\ & - \boldsymbol{u}_s^{\mathrm{II}}(r, \varphi, z) \cos\psi \sin\theta - [\boldsymbol{u}_s^{\mathrm{III}}(r, \varphi, z) + \boldsymbol{u}_s^{\mathrm{IV}}(r, \varphi, z)] \sin\psi \sin 2\theta \end{aligned} \quad (1)$$

where $\boldsymbol{u}_s$ may represent displacement, velocity or acceleration depending on the type of source function. For $J=\mathrm{I}$, $q=1$ and $J=\mathrm{II}$, $q=2$, it reads,

$$\boldsymbol{u}_s^J(r, \varphi, z) = \begin{pmatrix} B_s(r, z) \sin q\varphi \\ C_s(r, z) \cos q\varphi \\ F_s(r, z) \sin q\varphi \end{pmatrix} \quad (2)$$

and for $J=\mathrm{III}$, $q=2$ and $J=\mathrm{IV}$, $q=0$,

$$\boldsymbol{u}_s^J(r, \varphi, z) = \begin{pmatrix} A_s(r, z) \cos q\varphi \\ D_s(r, z) \sin q\varphi \\ E_s(r, z) \cos q\varphi \end{pmatrix} \quad (3)$$

where q is the azimuth angle factor, which depends on types of simple

source, B_s, A_s; C_s, D_s; E_s, F_s are radial, transverse and vertical components, respectively, and

$$\left.\begin{aligned} A_s &= B_s = \Pi(r) \\ C_s &= D_s = \Pi(\varphi) \\ E_s &= F_s = \Pi(z) \end{aligned}\right\} \tag{4}$$

where

$$\Pi(m) = \frac{D_0}{4\pi\beta^2} \sum_{n=1}^{4} \frac{\beta^n}{R^n} [P_{n\alpha}(m) f^{(2-n)}(t-t_\alpha) + P_{n\beta}(m) f^{(2-n)}(t-t_\beta)], \quad m = r, \varphi, z \tag{5}$$

where $t_\alpha = R/\alpha$, $t_\beta = R/\beta$, $R^2 = r^2 + z^2$; $\alpha = \sqrt{(\lambda+2\mu)/\rho}$ and $\beta = \sqrt{\mu/\rho}$ are longitudinal and transversal wave velocities, respectively. λ and μ are Lamé constants. In this paper we let $\lambda = \mu$. The radiant factors $P_{nc}(m)$ for $\lambda = \mu$ are shown in the appendix. $\boldsymbol{u}_s^{\mathrm{I}}$, $\boldsymbol{u}_s^{\mathrm{II}}$, $\boldsymbol{u}_s^{\mathrm{III}}$ and $\boldsymbol{u}_s^{\mathrm{IV}}$ express four basic simple point sources. They are:

Source I the dip slip on a vertical fault plane.
Source II the strike slip on a vertical fault plane.
Source III asymmetrical component of horizontal tensile fracture on a vertical fault plane.
Source IV the sum of symmetric component of horizontal tensile fracture on a vertical fault plane and vertical tensile fracture on a horizontal fault plane.

The seismic waves radiated from any point source with arbitrary slip angle and arbitrary dip angle of the fault can be obtained by combining those of the four simple sources. In our analyses, the source III and IV are neglected by assuming a vertical fault plane of the Ninghe earthquake.

Another important virtue of the rewritten representation formulas is the reduction of three dimensional problems into two dimensional ones by separating coodinate φ from r and z. Obviously, this can save memory and computational time, since only two dimensional functions need to be computed, although there still remain three components in the whole problem (see Eq. 10).

A vertical rectangular plane fault is assumed as the source of the Ninghe earthquake. Fig. 9 shows a schematic display of fault geometry as well as observation stations. The fault is divided into square subfaults with equal side lengths of 2.5 km. A point source is placed at the center of each subfault. The rupture starts from the hypocenter located at the center of the fault plane, then spreads radiantly. The rupture speed is assumed to be constant. Synthetic accelerograms from

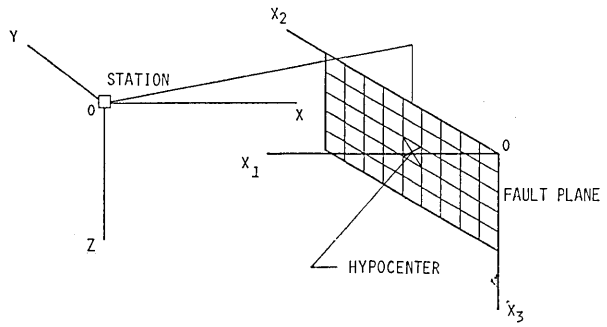

Fig. 9. Schematic picture of the fault model and observation station. The fault is divided into equal subfaults and a point source is placed at the center of each subfault. In computing synthetic accelerograms due to a point source, the origin of source coodinates is located at the center of each subfault.

both the strike and dip slips are computed. The total accelerograms have been obtained by superposing the contributions from each point source. Some other rupture processes, such as unidirectional or bilateral ruptures, have been adopted to find the most suitable source process. No significant difference has been found among them for simulating ground motions of the Ninghe earthquake.

Instead of displacement or velocity, we simulate time histories of ground acceleration using an acceleration source function. The acceleration source function is shown in Fig. 10 as well as the corresponding displacement and velocity waveforms. It may be expressed by the following formulas:

$$
\begin{aligned}
F_a(t) &= F(t) - F(t-T_d) \\
F(t) &= 16\,t^3 && 0 \leqslant t \leqslant 0.25\,T_0 \\
&= 1 - 48\left(t - \frac{T_0}{2}\right)^2 t && 0.25\,T_0 \leqslant t \leqslant 0.5\,T_0 \\
&= 1 + 48\left(t - \frac{T_0}{2}\right)^2 (t - T_0) && 0.5\,T_0 \leqslant t \leqslant 0.75\,T_0 \\
&= -16(t-T_0)^3 && 0.75\,T^0 \leqslant t \leqslant T_0 \\
&= 0 && t<0,\quad t>T_0
\end{aligned}
\qquad (6)
$$

Where T_0 is the duration of acceleration or deceleration impulse, and T_d is the delay time of deceleration impulse. In fact, it consists of acceleration and deceleration impulses, Generally speaking, T_0 is not equal to T_d, the height and duration of acceleration impulse is not equal to that of deceleration impulse. Moreover, the whole process may include several subfaulting processes (SATO, R., 1984), namely, the whole process

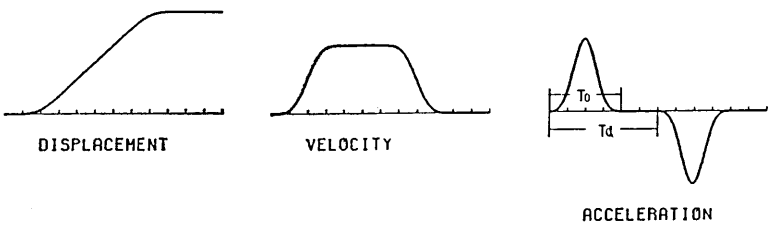

Fig. 10. An acceleration time source function used in this paper. The function consists of a acceleration and a deceleration impulse. The T_o is the duration of the impulse and the T_d is the delay time of the deceleration impulse. For simplifying analyses, the height and the period of acceleration and deceleration impulses are assumed to be equal. The corresponding velocity and displacement waveforms are also shown in this figure.

may include several acceleration and deceleration processes with different heights and durations. For ease in computation, however, we assume that both the acceleration and deceleration impulses have the same height and duration at each subfault. The time interval between the peak values has the same order as the rise time of the ramp displacement source function usually used in many studies.

5. Medium Model

The crustal structure the of Beijing-Tianjin-Tangshan area has been studied from several industry explosions and some data of earthquake observation (TENG *et al.*, 1979). The results are shown in Table 3. The hypocenter of the Ninghe earthquake is located in the second layer and the fault may extend into the third layer, but we assume the second layer extends into infinity in the simulation. As will be shown later, this approximation does not affect accelerograms significantly.

Fig. 11 shows the bottom surface bathymetric lines of the Quaternary system in the Beijing-Tianjin-Tangshan area (LI, 1982). According to the figure, it is difficult to conclude that the upper ground structure of this area is laterally homogeneous. The depths of base rock are not

Table 3. Velocity structure of the Beijing-Tianjin-Tangshan-Zhangjiakou area.

Thickness (km)	*P*-velocity (km/sec)	*S*-velocity (km/sec)
5.3	4.52	2.61
14.4	5.91	3.44
16.7	6.83	3.87
∞	7.99	4.60

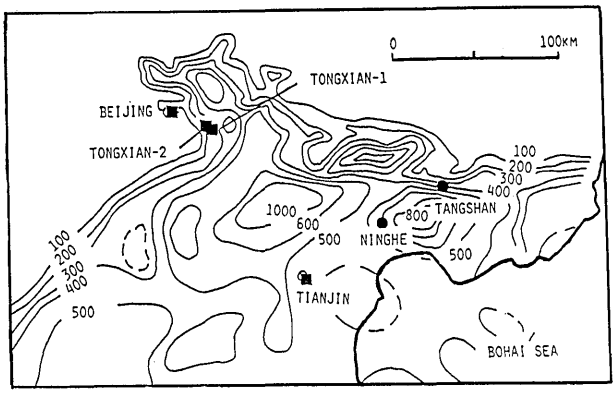

Fig. 11. The bottom surface bathymetric lines of the Quaternary system in the Beijing-Tianjin-Tangshan area (from LI, 1982). It shows that the depths of base rock under the observation stations are all different. The two Tongxian stations are located in the region, where the depth of base rock changes rapidly.

uniform. It may be about 100 m at the Beijing station and about 500 m at the Tianjin station. The two Tongxian stations are situated in the region where the depth of base rock changes rapidly from 200 m to 400 m. Therefore lateral heterogeneity of ground structure should be taken into account within the frequency range under consideration in simulating ground motions of Tongxian stations. On the other hand, it is not necessary to take a laterally heterogeneous ground structure model for all stations, because these stations are quite far from each other except for the two Tongxian stations. The scattering waves on the interface of the base rock at one station will arrive in later accelerograms at another station. As indicated earlier, it is satisfactory to simulate only the direct path S wave and its reflecting, refracting or scattering waves due to discontinued interfaces of ground structures near the stations. In fact, the unified ground structure model requires too heavy computational work to complete in an acceptable CPU time. A suitable approach to overcome the difficulty is to provide different ground structure model for different stations considering the local site condition. Therefore, three medium models are proposed for the four stations in this paper (Fig. 12). The model-1 is for Tianjin, the model-3 is for Beijing and the model-2 is for the Tongxian stations. In fact, the base rock under the Tongxian stations does not dip vertically, but for the sake of simplifying the analysis we assume a vertical interface as the first approximation to interpret the principal features of the observed ground motions.

Only shallow boring data ($h \leqslant 70$ m) near the stations and some results of seismic prospecting tests are available for understanding the velocity structure of the upper sediment layers (PENG, personal communication,

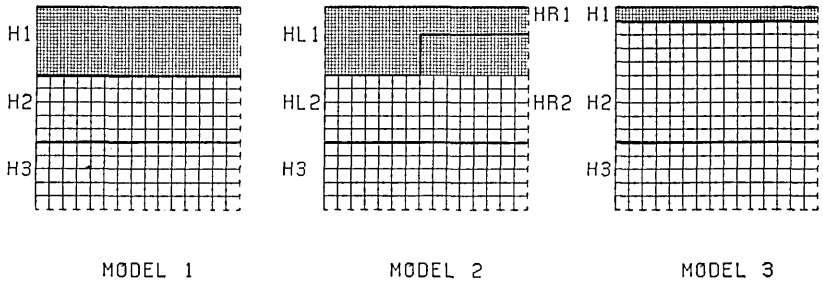

Fig. 12. Ground structure models of observation stations. The model-1 is for the Tianjin station, the model-3 is for the Beijing station and the model-2 is for the Tongxian stations, in which a vertical interface is introduced to study effects of lateral heterogeneity of ground stucture. Elastic parameters and thickness of each layer are shown in Table 4. Different mesh sizes between slow and high velocity layers are to guarantee computational accuracy and save cost of computation.

Table 4. Elastic parameters of the ground structure models.

		Model 1	Model 2	Model 3
Depth (km)	$H1$	0.5	$HL1$ 0.5 $HR1$ 0.2	0.1
	$H2$	4.8	$HL2$ 4.8 $HR2$ 5.1	5.2
	$H3$	∞	∞	∞
Density (kg/m^3)	$\rho 1$	2.0	2.0	2.0
	$\rho 2$	2.6	2.6	2.6
	$\rho 3$	2.8	2.8	2.8
P-wave velocity (m/s)	V_p1	1038.0	692.0	346.0
	V_p2	4520.0	4520.0	4520.0
	V_p3	5960.0	5960.0	5960.0
S-wave velocity (m/s)	V_s1	600.0	400.0	200.0
	V_s2	2610.0	2610.0	2610.0
	V_s3	3440.0	3440.0	3440.0

1985). To save computational labour we use a simple sediment soil sitting on the base rock. Since the soil includes many soil layers, we have to assume average values of elastic parameters for the layers. Then they are adjusted by fitting synthetic accelerograms to the observed ones. The final results are shown in Table 4.

6. Finite Difference Method

In the following parts, we call all of waves reflected or refracted by discontinued interfaces and scattered at heterogeneous region of mediums as scattering waves and are denoted by $\boldsymbol{u}$. The total seismic ground waves denoted by $\boldsymbol{u}_t$ are the sum of the waves radiated by the source, which are denoted by $\boldsymbol{u}_s$, and $\boldsymbol{u}$.

$$\boldsymbol{u}_t=\boldsymbol{u}_s+\boldsymbol{u} \tag{7}$$

The scattering waves $\boldsymbol{u}$ may also be written by separating the coordinates as follows:
for source I ($q=1$) and source II ($q=2$),

$$\boldsymbol{u}(r,\varphi,z)=\begin{pmatrix} B(r,z)\sin q\varphi \\ C(r,z)\cos q\varphi \\ F(r,z)\sin q\varphi \end{pmatrix} \tag{8}$$

for source III ($q=2$) and source IV ($q=0$),

$$\boldsymbol{u}(r,\varphi,z)=\begin{pmatrix} A(r,z)\cos q\varphi \\ D(r,z)\sin q\varphi \\ E(r,z)\cos q\varphi \end{pmatrix} \tag{9}$$

where two dimensional functions satisfy the following equations of motion for source I ($q=1$) and source II ($q=2$)

$$\left.\begin{aligned}
\frac{\partial^2 B}{\partial t^2}&=\alpha^2\left[\frac{\partial^2 B}{\partial r^2}+\frac{1}{r}\frac{\partial B}{\partial r}-\frac{B}{r^2}+\frac{q}{r^2}C-\frac{q}{r^2}\frac{\partial C}{\partial r}+\frac{\partial^2 F}{\partial r\partial z}\right]\\
&\quad+\beta^2\left[-\frac{q}{r^2}C+\frac{q}{r}\frac{\partial C}{\partial r}-\frac{q^2}{r^2}B+\frac{\partial^2 B}{\partial z^2}-\frac{\partial^2 F}{\partial r\partial z}\right]\\
\frac{\partial^2 C}{\partial t^2}&=\alpha^2\left[\frac{q}{r}\frac{\partial B}{\partial r}+\frac{q}{r^2}B-\frac{q^2}{r^2}C+\frac{q}{r}\frac{\partial F}{\partial z}\right]\\
&\quad+\beta^2\left[\frac{\partial^2 C}{\partial z^2}+\frac{\partial^2 C}{\partial r^2}+\frac{1}{r}\frac{\partial C}{\partial r}-\frac{C}{r^2}-\frac{q}{r}\frac{\partial F}{\partial z}-\frac{q}{r}\frac{\partial B}{\partial r}+\frac{q}{r^2}B\right]\\
\frac{\partial^2 F}{\partial t^2}&=\alpha^2\left[\frac{\partial^2 B}{\partial r\partial z}+\frac{1}{r}\frac{\partial B}{\partial z}-\frac{q}{r}\frac{\partial C}{\partial z}+\frac{\partial^2 F}{\partial z^2}\right]\\
&\quad+\beta^2\left[\frac{\partial^2 F}{\partial r^2}+\frac{1}{r}\frac{\partial F}{\partial r}+\frac{q}{r}\frac{\partial C}{\partial z}-\frac{q^2}{r^2}F-\frac{\partial^2 B}{\partial r\partial z}-\frac{1}{r}\frac{\partial B}{\partial z}\right]
\end{aligned}\right\} \tag{10}$$

For source III ($q=2$) and source IV ($q=0$), it is necessary only to change functions B, C, F to A, $-D$, E in the above equations.

By substituting central difference formulas for every differential

term of Eq. (10), and with proper boundary conditions on symmetric axis and interfaces, the whole problem can be solved by the finite difference method. References of algorithm formulas corresponding to each type of grids used in this paper are shown in Table 5.

Table 5. Reference to finite difference algorithms.

Part of model	Equations used
interior points	ALTERMAN *et al.*, 1972
conner points	FUYUKI *et al.*, 1980
horizontal interfaces	ALTERMAN *et al.*, 1972
vertical interface	this paper
transmitting boundaries	LIAO *et al.*, 1984a
symmetric axis	YUAN *et al.*, 1984

As shown in Eq. (7), total waves can be divided into two parts, that is waves radiated by the source and waves scattered at interfaces, so that we may divide a whole computational region into two parts: interior region A-B-B′-A′ and boundary region C-D-D′-C′ (Fig. 13). Assuming the total waves of the interior region and the scattering waves of the boundary region are known at $(p-1)\Delta t$ and $p\Delta t$, for obtaining waves of the interior region at the next instant $(p+1)\Delta t$, it is necessary to add incident waves radiated by the source on the line C-C′. Similarly, it is necessary to subtract incident waves radiated by the source from those on the line B-B′ for computing the scattering waves of the boundary region C-D-D′-C′. In terms of this scheme we do not have to compute seismic waves from the source, which costs too much and sometimes leads to dispersion.

The broken lines in Fig. 12 indicate the transmitting boundaries,

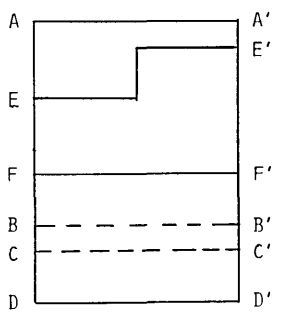

Fig. 13. The computational model. A-A′ is the surface ground. E-E′ and F-F′ are layer interfaces. B-C-C′-B′ is input region, D-D′ is a transmitting boundary at bottom.

introduced for modeling the radiation conditions of an infinite region at fictitious boundaries. The unified transmitting boundary method (LIAO *et al.* 1984a, 1984b) is applied to deal with the boundaries in this paper. This method can transmit elastic waves with any incident angle out of the transmitting boundary under the accuracy required and can be easily incooperated with the numerical method of transient wave analyses.

In the above model, the whole computational region must include the symmetric axis, on which the source is located, and the observation stations. If the epicentral distance is very long and the size of mesh is small for ensuring a certain accuracy, it will require tremendous computational work, even if for a point source. A modified method is to divide the whole region into several subregions (Fig. 14). At first, the subregion including the symmetric axis is computed for sufficient duration, while values on the right boundary (transmitting boundary) are stored at every

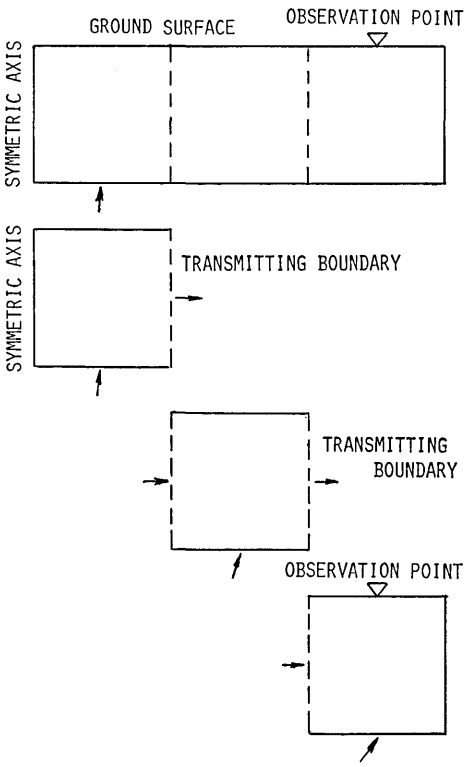

Fig. 14. Schematic picture of computational model, in which the total computational region is divided into several small regions. Computation is conducted region by region sequentially. The output values of the right boundary are put to memory as the input of the left boundary for the next region.

time step. Then the second subregion is computed, while those values stored in the computation of the left subregion are taken as the input at corresponding grids of the left side boundary, and those values of grids in the right boundary are also stored again for the input of the next subregion. Sequentially, computation is continued until the necessary results are obtained. This method can save memory storage and omit unnecessary computational labour, on the waves which have not arrived or have passed out of the region. Another approach is to compute only one region which includes the observation station. The left side boundary is treated, say, as a transmitting boundary. By comparing the resulted waves with those of exact resolution obtaining by the full computation in the whole region, we can find a column of grids, whose peak value and waveform approximate the exact resolution with accuracy required. So only those synthetic accelerograms of grids being located right of the selected grid are acceptable for simulation.

Another important factor to guarantee successful computation is to select space and time increment (Δr and Δt) (SATÔ, Y. *et al.*, 1983). After some numerical tests, we have found Satô's result of two dimensional analyses is still suitable for our problem. Since the small mesh size will bring computational costs too high, one compromise between saving computational cost and getting better accuracy is to use the small size for slow velocity layers and the large size for high velocity layers (Fig. 12). The values of small grids at the interface are obtained by linear interpolation from those of large grids. In our computation $\Delta r=50$ m and 200 m, $\Delta t=0.01$ sec are selected for model-1, $\Delta r=25$ m and 100 m, $\Delta t=0.005$ sec are for model-2 and model-3.

7. Results and Discussion

1. Character of synthetic accelerograms.

Fig. 15 illustrates an example of synthetic acceleration time histories derived for a strike slip point source with only an acceleration impulse source function at the hypocenter for Tianjin. In this figure, A-A′ is the ground surface, E-E′ and F-F′ are layer interfaces. It can be seen from this figure that the first interface gives rise to stronger reflecting waves than the second interface, since the impedance ratio between the upper two layers is greater than that between the two lower layers. Therefore, it may not produce considerable error if deep crustal layers are neglected in the simulation.

A strike slip source produces quite different ground motions than that of a dip slip source, if the epicentral distance is about 50 kilometers. The transverse component of ground acceleration is more predominant

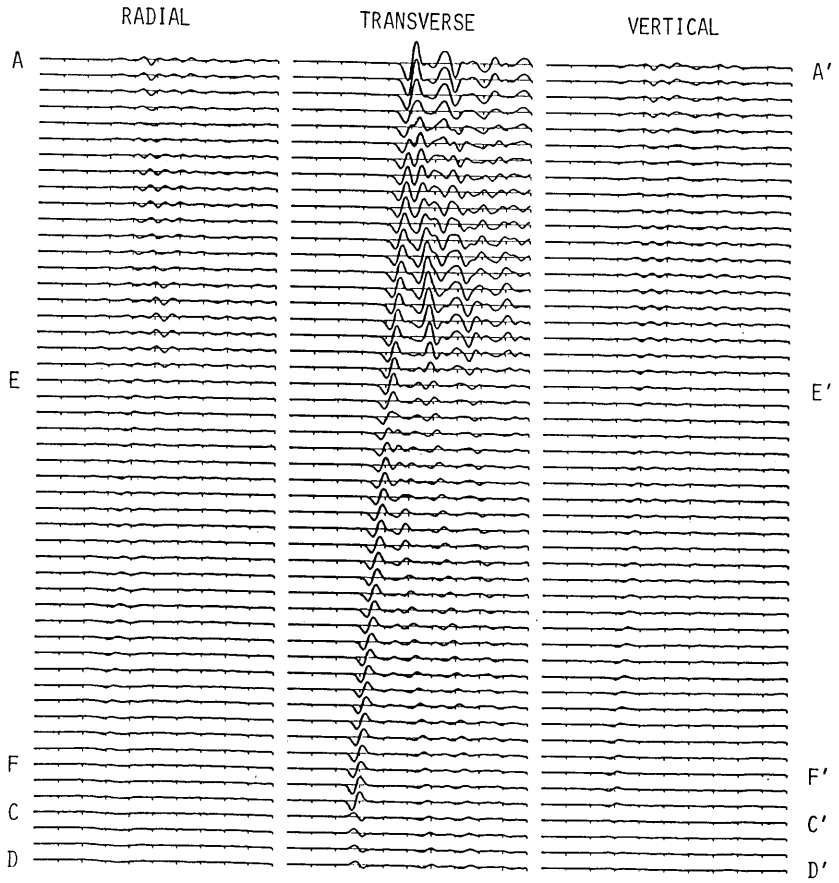

Fig. 15. An example of synthetic acceleration time histories at different depths. The source is a strike slip point source at the hypocenter with only acceleration impulse source function. A-A′ is the ground surface, E-E′, F-F′ are layer interfaces. Waves on C-D-D′-C′ are scattered waves. The mesh sizes are different actually between A-E-E′-A′ and E-D-D′-E′ (Fig. 12), although they are the same in this figure.

than radial and vertical ones and its waveform is a rather simple like pulse shape for strike slip sources (Fig. 16). On the contrary, for dip slips the transverse component is weaker than radial and vertical ones, which have more complicated waveforms (Fig. 17). To harmonize with the observed records, it must be assumed that strike slips are more predominant than dip slips on the fault of the Ninghe earthquake. Meanwhile, the parameter T_0 and T_d of source function should be selected suitably in order to produce the large pulse shaped waves which appear in the observed records.

The other sensitive parameter affecting synthetic accelerograms is

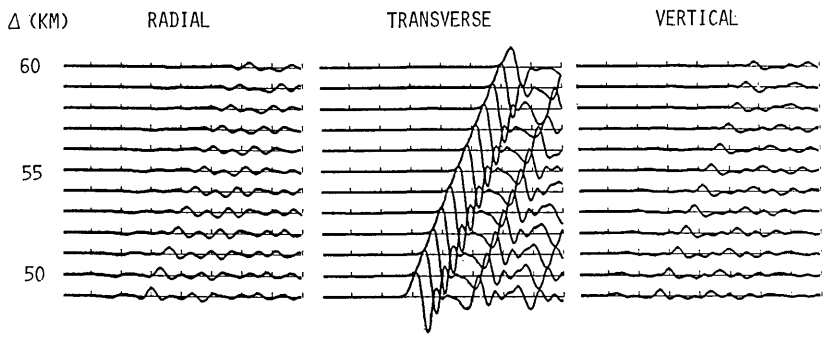

Fig. 16. An example of synthetic time histories of ground acceleration in epicentral distances of about 50 km for a strike slip point source with only acceleration impulse source function. The transverse component is greater than radial and vertical ones.

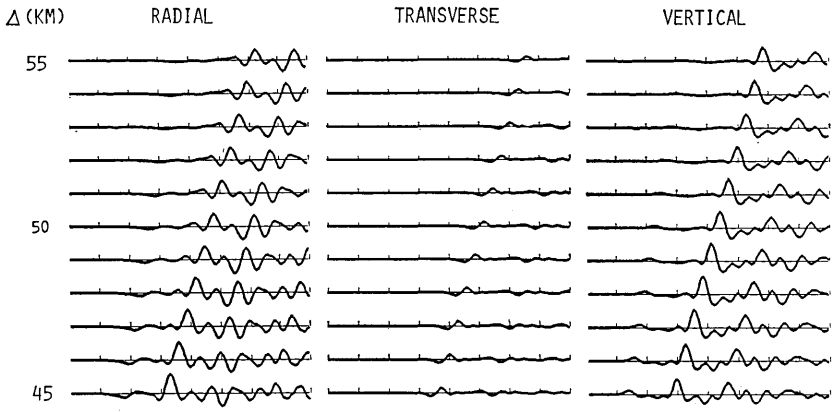

Fig. 17. An example of synthetic time histories of ground acceleration in epicentral distances of about 50 km for a dip slip point source with only acceleration impulse source function. The transverse component is smaller than radial and vertical ones.

the rupture speed. Although the final results show the Ninghe earthquake to be like a large point source, a slight change of rupture speed gives rise to a considerable variety of synthetic acceleration waveforms.

2. Comparison of acceleration time histories

Synthetic accelerograms resulting from the above simulating process are compared with cooresponding observed waveforms in Fig. 18. All of these accelerograms are aligned according to the arrival time of the first *S*-wave. The amplitude scale is so adjusted as to make the peak value

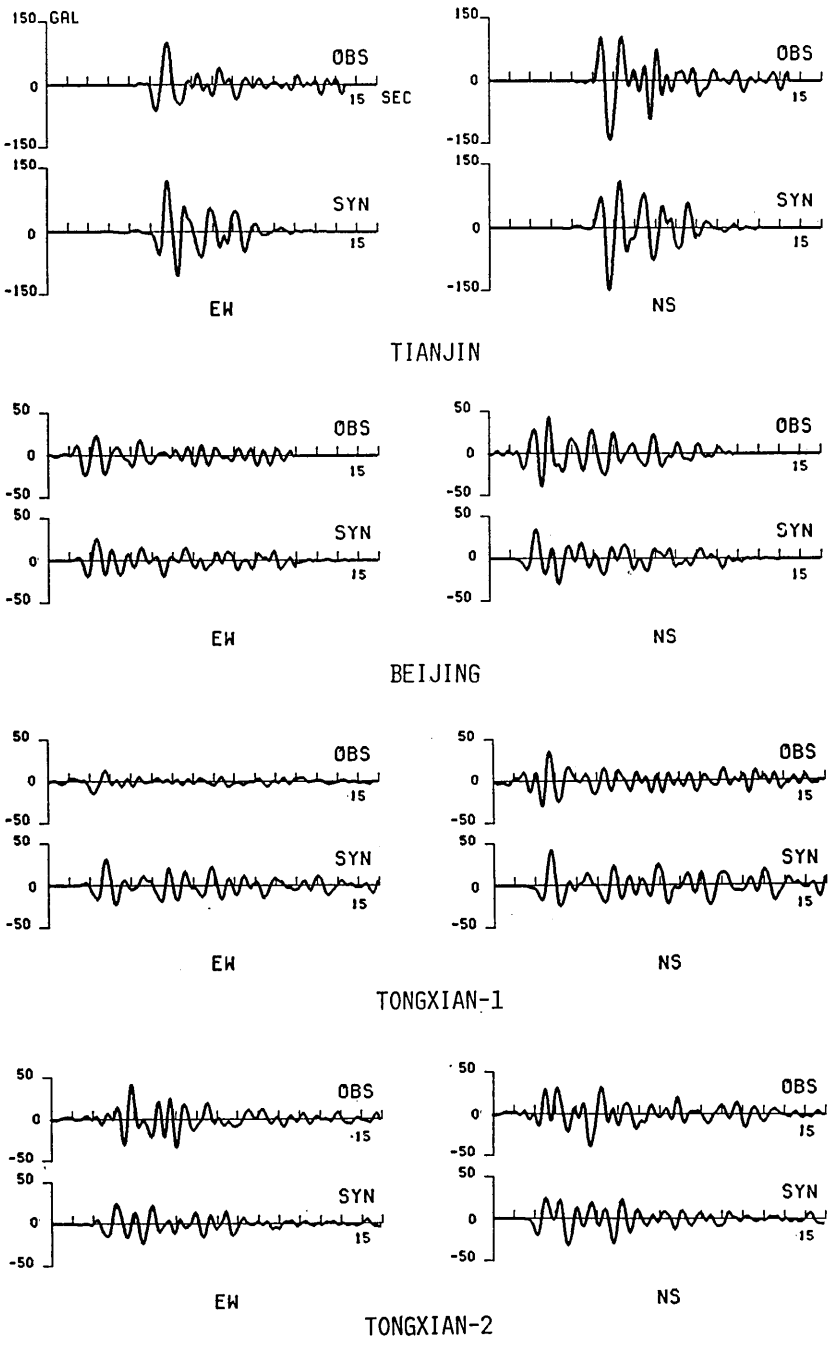

Fig. 18. Comparison between the synthetic accelerograms and filtered accelerograms of the 1976 Ninghe earthquake. All components are aligned according to the first S-wave arrival. The amplitude scales are aligned by fitting the synthetic maximum acceleration of the NS component of Tianjin accelerograms to the observed one.

in synthetic accelerogram of the NS component equal to that observed at Tianjin station.

There is no universal method for assigning a quantitative measure of goodness of fit between synthetic and observed data (ARCHULETA, 1984). The criterion for measuring goodness of fit may depend on the purpose of the individual research. We have also used visual comparison and physical reasoning in time domain.

The large pulse shaped waveforms in all of these accelerograms are successfully simulated, except for the EW component of Tongxian-2, and the maximum amplitudes observed are also successfully simulated, except for the EW component of the Tongxian-1. It is difficult to duplicate all the aspects of recorded accelerograms, since the fault and medium models are not sufficiant in detail. But waveforms following the large pulse are similar in a gross sense, so general aspects of the synthetic accelerograms may agree well with the observed data. At the Tianjin station, the duration of synthetic accelerograms is shorter than that of observed ones, since we did not compute them for sufficient duration.

The vertical interface in model-2 (Fig. 12) does bring out a large difference between the synthetic accelerograms of the two Tongxian stations, which can not be expected from a laterally homogeneous layer model. Synthetic accelerograms and observed ones are very similar, especially in NS components, which indicates that model-2 reflects the principal property of ground structure at the Tongxian stations.

3. Faulting process

After trying more than hundreds of fault models, the most appropriate fault parameters, that is, the delay time of the deceleration impulse, T_d, the maximum acceleration, A_{max}, the ratio of dip slip to strike slip and rupture speed, V_r are shown in Table 6. Fig. 19 illustrates the distribution of maximum acceleration on the fault, that is, the peak value of source function in each subfault.

Fig. 19 indicates that the energy was released in a small region surrounding the hypocenter, like the Coyote Lake earthquake of Aug. 1979, U.S.A. (LIU *et al.*, 1983). The simulation of the Ninghe earthquake shows that seismic waves radiated by a simple mechanism of source will become very complicated due to reflection and scattering of waves in ground structure at the recording site. For simulating strong ground motions in a short period range, not only the rupture process on the fault must be considered, but also the effects of ground structures, particularly lateral heterogeneity of the recording site ground structure, should be studied in detail.

As mentioned earlier, the strike slips were more predominant than

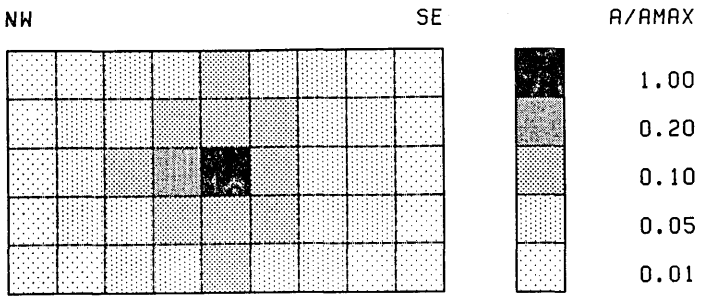

Fig. 19. The distribution of maximum acceleration of every source on the fault. It shows that the energy may be released in a small region surrounding the hypocenter.

Table 6. Fault parameters of the Nov. 15, 1976 Ninghe earthquake.

fault length, L	22.5 km
fault width, W	12.5 km
period of acceleration impulse, T_0	1.0 sec
delay time of deceleration impulse, T_d	0.25 sec
maximum acceleration, A_{max}	3.38 g
dip slip/ strike slip	0.1
rupture speed, V_r	2.8 km/sec

the dip slips on the fault of the Ninghe earthquake, since the ratio of the former to the latter is only 0.1.

Although several observed data in earthquake areas show that the maximum ground acceleration exceeds 1 g, up to now there is no observed data to tell how large the maximum acceleration is on the fault. Some studies of simple dynamic rupture models propose that the maximum acceleration on the fault may become 1 g or 2 g under certain assumptions (BRUNE, 1970; IDA, 1973). We estimated the maximum acceleration on the fault at about 3 g, by fitting the synthetic peak value to the observed records in Tianjin. This value will be corrected by further studies, since the model used in our simulation is simple and the nonlinearity of source region is not considered.

4. Comparison of response spectra

From the comparison of acceleration response spectra (Fig. 20), it may be concluded that most response spectra fit well in peak values and spectral shapes. In the spectra of NS component at Beijing, there are peak values at about a period of 2 seconds. It is identical to the predominant period of ground being calculated from the formula $T=4H/v$ (KANAI, 1969). The T is the predominant period of a layer under the

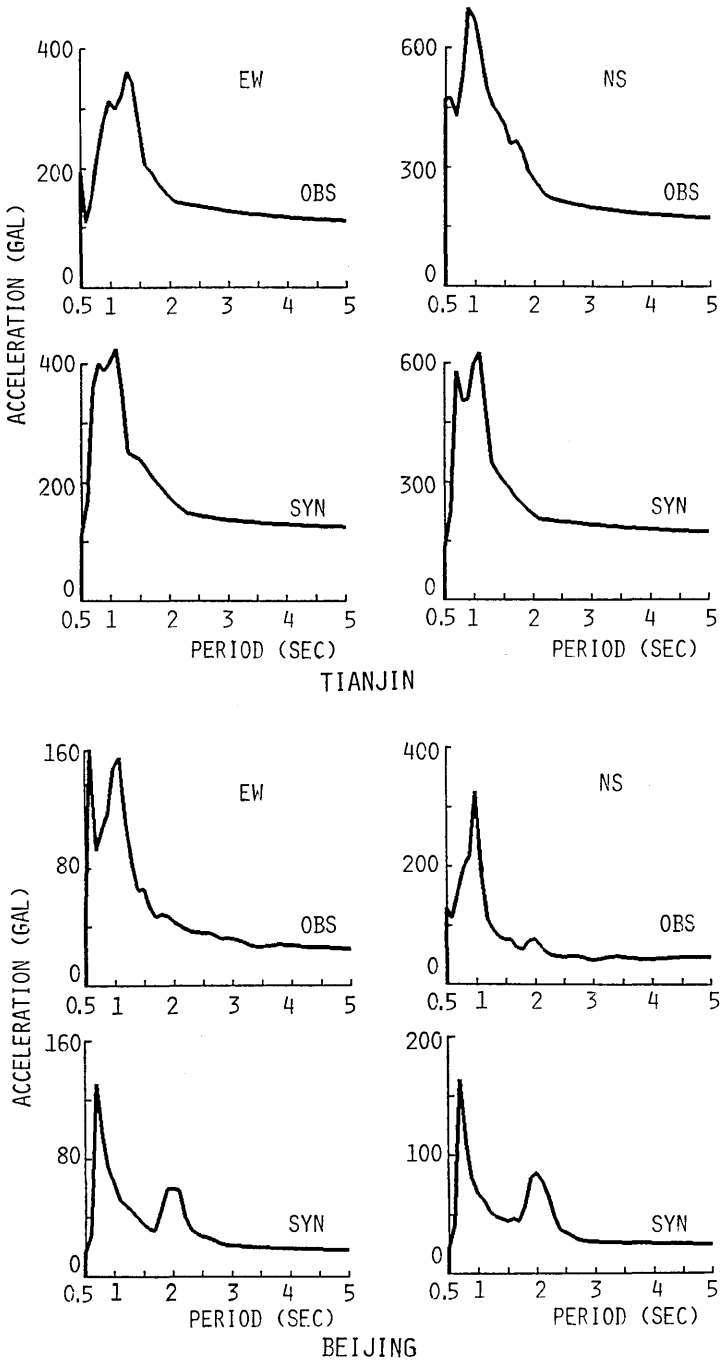

Fig. 20-1. Comparison of acceleration response spectra between the synthetic and filterd accelerograms of the 1976 Ninghe earthquake.

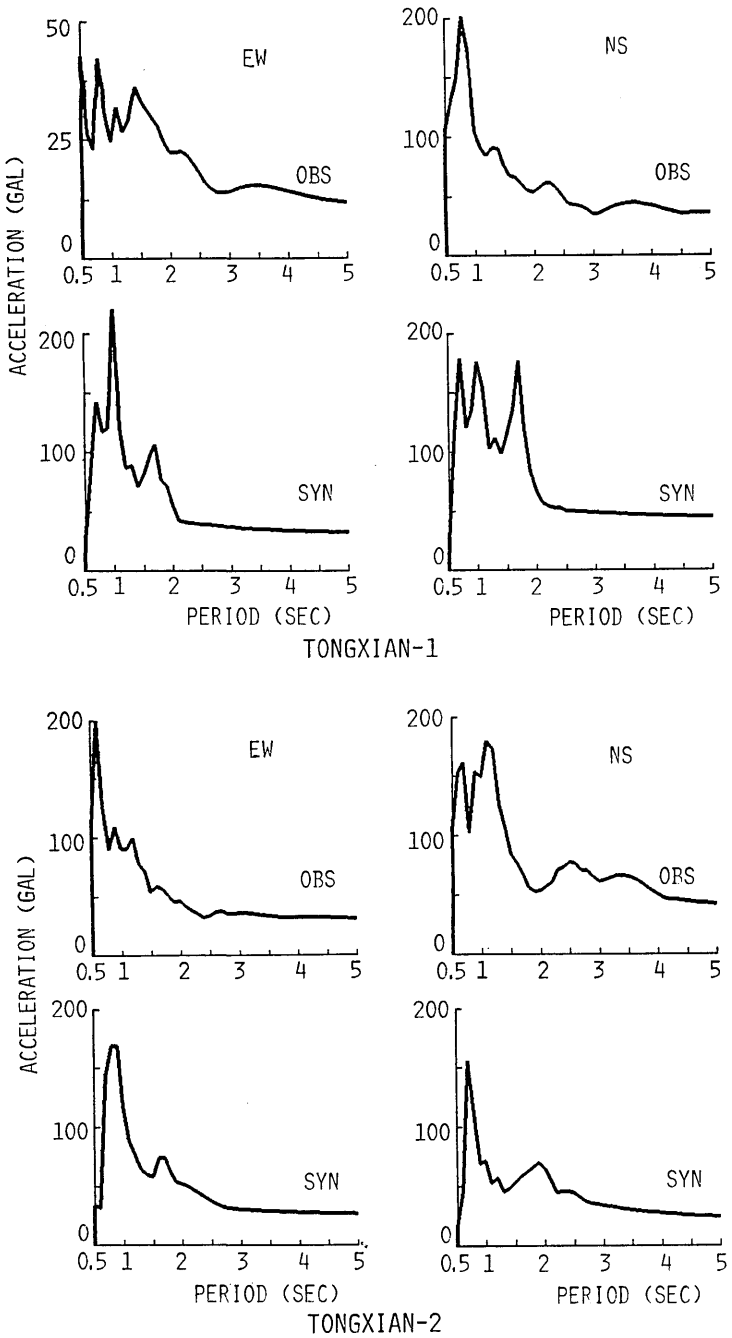

Fig. 20-2. Comparison of acceleration response spectra between the synthetic and filtered accelerograms of the 1976 Ninghe earthquake.

normal impinging of the *SH* wave, H is the thickness of the layer and v is the S wave velocity. It also indicates that strike slips were predominant in the Ninghe earthquake, because strike slips produce a large transverse component of ground motions (Fig. 16), which are *SH* motions. Similar to the discussions in the time domain, some disagreement between synthetic and observed spectra of Tongxian records is found. More realistic ground structure models are necessary to give a better fit.

8. Summary

Based on a close investigation of observed accelerograms of the 1976 Ninghe, China earthquake, some assumptions on the source function and rupture process are proposed. With several measures of saving computational labour and memory storage, synthetic accelerograms are computed by the finite difference method and compared with the low-passed observed accelerograms. By the trial and error process, parameters of the fault and distribution of peak acceleration on the fault are deduced.

According to our simulation of seismic ground motions, the construction of suitable medium models is found to be a key problem for successful simulation. In some cases, the lateral heterogeneity of the recording site ground structure should not be neglected in the short period range. As shown in the Ninghe earthquake, complex seismic ground motions will be produced due to ground structure, although the rupture process is simple.

Our method for synthesizing theoretical seismograms may be useful for analyzing near-field strong ground motions in the region close to the epicenter, since it can compute both near- and far-field terms, as well as all types of waves. But the effects of dissipation in wave propagation should be taken into account in the short period range (SATO, R., 1984). This effect is neglected in our simulation.

9. Acknowledgments

We are grateful to Prof. Minami for his thoughtful review of the manuscript and for offering valuable comments and suggestions. We are also thankful to Dr. Miyatake for helpful discussions and to Mr. Koketsu and Miss. Kotake for their kind help in computational work.

Appendix

Azimuth radiant factor $P_{nc}(m)$ of Eq. (5)

type of source \ nc / m		1α	1β	2α	2β	3α
I	r	$\frac{2}{\bar{\alpha}^3}\frac{r^2 z}{R^3}$	$\frac{z}{R}\left(1-2\frac{r^2}{R^2}\right)$	$\frac{2}{\bar{\alpha}^2}\frac{z}{R}\left(6\frac{r^2}{R^2}-1\right)$	$3\frac{z}{R}\left(1-4\frac{r^2}{R^2}\right)$	$\frac{6}{\bar{\alpha}}\frac{z}{R}\left(5\frac{r^2}{R^2}-1\right)$
	φ	0	$\frac{z}{R}$	$-\frac{2}{\bar{\alpha}^2}\frac{z}{R}$	$3\frac{z}{R}$	$-\frac{6}{\bar{\alpha}}\frac{z}{R}$
	z	$\frac{2}{\bar{\alpha}^3}\frac{rz^2}{R^3}$	$\frac{r}{R}\left(1-2\frac{z^2}{R^2}\right)$	$\frac{2}{\bar{\alpha}^2}\frac{r}{R}\left(6\frac{r^2}{R^2}-1\right)$	$3\frac{r}{R}\left(1-4\frac{r^2}{R^2}\right)$	$\frac{6}{\bar{\alpha}}\frac{z}{R}\left(5\frac{r^2}{R^2}-1\right)$
II	r	$\frac{1}{\bar{\alpha}^3}\frac{r^3}{R^3}$	$\frac{r}{R}\left(1-\frac{r^2}{R^2}\right)$	$\frac{2}{\bar{\alpha}^2}\frac{r}{R}\left(3\frac{r^2}{R^2}-1\right)$	$3\frac{r}{R}\left(1-2\frac{r^2}{R^2}\right)$	$\frac{3}{\bar{\alpha}}\frac{r}{R}\left(5\frac{r^2}{R^2}-1\right)$
	φ	0	$\frac{r}{R}$	$-\frac{2}{\bar{\alpha}^2}\frac{r}{R}$	$3\frac{r}{R}$	$-\frac{6}{\bar{\alpha}}\frac{r}{R}$
	z	$\frac{1}{\bar{\alpha}^3}\frac{r^2 z}{R^3}$	$-\frac{r^2 z}{R^3}$	$\frac{6}{\bar{\alpha}^2}\frac{r^2 z}{R^3}$	$6-\frac{r^2 z}{R^3}$	$\frac{15}{\bar{\alpha}}\frac{r^2 z}{R^3}$
III	r	$\frac{1}{2\bar{\alpha}^3}\frac{r^3}{R^3}$	$\frac{1}{2}\frac{r}{R}\left(1-\frac{r^2}{R^2}\right)$	$\frac{1}{\bar{\alpha}^2}\frac{r}{R}\left(3\frac{r^2}{R^2}-1\right)$	$\frac{3}{2}\frac{r}{R}\left(1-2\frac{r^2}{R^2}\right)$	$\frac{3}{2\bar{\alpha}}\frac{r}{R}\left(5\frac{r^2}{R^2}-1\right)$
	φ	0	$-\frac{1}{2}\frac{r}{R}$	$\frac{1}{\bar{\alpha}^2}\frac{r}{R}$	$-\frac{3}{2}\frac{r}{R}$	$\frac{3}{\bar{\alpha}}\frac{r}{R}$
	z	$\frac{1}{2\bar{\alpha}^3}\frac{r^2 z}{R^3}$	$-\frac{1}{2}\frac{r^2 z}{R^3}$	$\frac{3}{\bar{\alpha}^2}\frac{r^2 z}{R^3}$	$-3\frac{r^2 z}{R^3}$	$\frac{15}{2\bar{\alpha}}\frac{r^2 z}{R^3}$
IV	r	$\frac{1}{\bar{\alpha}^3}\frac{r}{R}\left(1-\frac{3}{2}\frac{r^2}{R^2}\right)$	$-\frac{3}{2}\frac{rz^2}{R^3}$	$\frac{1}{\bar{\alpha}^2}\frac{r}{R}\left(7-9\frac{r^2}{R^2}\right)$	$\frac{3}{2}\frac{r}{R}\left(6\frac{r^2}{R^2}-5\right)$	$\frac{9}{2\bar{\alpha}}\frac{r}{R}\left(4-5\frac{r^2}{R^2}\right)$
	z	$\frac{1}{\bar{\alpha}^3}\frac{z}{R}\left(1-\frac{3}{2}\frac{r^2}{R^2}\right)$	$\frac{3}{2}\frac{r^2 z}{R^3}$	$\frac{1}{\bar{\alpha}^2}\frac{z}{R}\left(4-9\frac{r^2}{R^2}\right)$	$3\frac{r}{R}\left(3\frac{r^2}{R^2}-1\right)$	$\frac{9}{2\bar{\alpha}}\frac{z}{R}\left(2-5\frac{r^2}{R^2}\right)$

$P_{3\beta}(m)=P_{4\beta}(m)=-\bar{\alpha}P_{3\alpha}(m)$, $P_{4\alpha}(m)=\bar{\alpha}P_{3\alpha}(m)$, $R^2=r^2+z^2$, $\bar{\alpha}=\frac{\alpha}{\beta}$

References

AKI, K., 1968, Seismic displacement near a fault, *J. Geophys. Res.*, **73**, 5359-5376.

AKI, K., 1982, Strong motion prediction using mathematical modeling techniques, *Bull. Seism. Soc. Am.*, **72**, (part. B), S29-S41.

ALTERMAN, Z. and D. LOEWANTHAL, 1972, Computer generated seismograms, *Methods in computational physics*, **12**, 35-164, Acad. press.

ARCHULETA, R. J., 1984, A fault model for the 1979 imperial valley earthquake, *J. Geophys. Res.*, **89**, 4559-4585.

BOORE, D. M., 1972, Finite difference methods for seismic wave propagation in heterogeneous materials, *Methods in computational physics*, **11**, 1-38, Acad. Press.

BOORE, D. M., 1983, Strong-motion seismology, *Reviews of Geophysics and Space Physics*, **4**, 1308-1318.

BOUCHON, M., 1982, The rupture mechanism of the Coyote Lake earthquake of August 6, 1979, inferred from near-field data, *Bull. Seism. Soc. Am.*, **72**, 745-758.

BRUNE, J. N., 1970, Tectonic stress and the spectra of seismic shear waves from earthquakes, *J. Geophys. Res.*, **75**, 4997-5009.

FUYUKI, M. and Y. MATSUMOTO, 1980, Finite difference analysis of Rayleigh wave scattering at a trench, *Bull. Seism. Soc. Am.*, **70**, 2051-2069.

HASKELL, N., 1969, Elastic displacement in the near-field of a propagating fault, *Bull. Seism. Soc. Am.*, **59**, 865-908.

HEATON, T. H. and D. V. HELMBERGER, 1979, Generalized ray models of the San Fernando earthquake, *Bull. Seism. Soc. Am.*, **69**, 1311-1341.

IDA, Y., 1973, The maximum acceleration of seismic ground motion, *Bull. Seism. Soc. Am.*, **63**, 959-968.

IMAKAWA, K., N. MIKAMI and T. MIKUMO, 1984, Analytical and semi-empirical syntheses of near-field seismic waveforms for investigating the rupture mechanism of major earthquake, *J. Phys. Earth*, **32**, 317-338.

ISHIKAWA, Y., C. Z. ZHU and T. Q. CAO, 1983, On some characteristics of strong aftershocks of the 1976 Tanshan, 1975 Haicheng and 1976 Yanyuan-Ninglang earthquakes, *Acta, Seismo. Sinica*, **5**, 15-30.

KANAI, K., 1983, Engineering Seismology, University of Tokyo press.

LI, X. G., 1982, The Bottom interface of the Quanternary System in the south of Yanshan mountain and the Hebei plain, its tectonic meaning, Field report, Institute of Geology SSB, China.

LIAO, Z. P., B. P. YANG and Y. F. YUAN, 1980, Effect of three-dimensional topograph on earthquake ground motion, *Proceedings of the seventh world conference on earthquake engineering*, **2**, 161-168.

LIAO, Z. P., H. L. WONG, B. P. YANG and Y. F. YAUN, 1984, A transmitting boundary for transient wave analyses, *Scientia Sinica, Series A*, **27**, 1063-1076.

LIAO, Z. P. and H. L. WONG, 1984, A transmitting boundary for the numerical simulation of elastic wave propagation, *Int. J. Soil, Dyn. Earthq. Eng.*, **3**, 174-184.

LIN, B. H., S. F. WU and Z. M. GAO, 1979, On the lowering of the epicentral intensity of the Ninghe aftershock of May 12, 1977, *Acta. Geophys. Sinica*, **22**, 14-24.

MARUYAMA, T., 1963, On the force equivalents of dynamic elastic dislocation with reference to the earthquake mechanism, *Bull. Earthq. Res. Inst., Univ. Tokyo*, **41**, 467-486.

MIKUMO, T., 1973, Faulting process of the San Fernando earthquake of February 9, 1971 inferred from static and dynamic near-field displacement, *Bull. Seism. Soc. Am.*, **63**, 249-269.

OLSON, A. H. and R. J. APSEL, 1982, Finite faults and inverse theory with applications to the 1979 Imperial Valley earthquake, *Bull. Seism. Soc. Am.*, **72**, 1969-2001.

SATO, R., 1984, Study on short-period behavior in fault motion and estimation of input seismic motion, Special Natural Disaster Research, No. A-59-3.

SATÔ, Y. and K. ISHIHARA, 1983, On the numerical calculation of wave propagation by the finite difference method, *Bull. Earthq. Res. Inst., Univ. Tokyo*, **58**, 163-173.

TENG, T. W., H. YAO and H. N. ZHOU, 1979, Crustal structure in the Beijing-Tianjin-Tangshan-Zhangjiakou region, *Acta Geophys. Sinica*, **22**, 218-236.

TRIFUNAC, M. D., 1974, A three-dimensional dislocation model for the San Fernando, California, earthquake of February 9, 1971, *Bull. Seism. Soc. Am.*, **64**, 149-172.

WONG, H. L. and M. D, TRIFUNAC, 1977, A note on the effects of recording site conditions on amplitudes of strong earthquake motion, *proceedings of the sixth world conference on earthquake engineering*, **1**, 452-457.

YUAN, Y. F. and Z. P. LIAO, 1984, Numerical solution of wave field near a dislocation

source in an elastic half-space, *Acta Seismo. Sinica*, **6**, 324-340.

ZAMA, S., 1981, Behavior of the elastic waves propagating through the irregular structures, I. Effect on cliff by earthquake ground motions, *Bull. Earthq. Res. Inst., Univ. Tokyo*, **56**, 741-752.

ZHANG, Z. L., Q. Z. LI, J. C. GU, Y. M. JIN, M. Y. YANG and W. Q. LIU, 1980, The fracture processes of the Tangshan earthquake and its mechanical analyses, *Acta Seismo. Sinica*, **2**, 112-129.

ZHAO, G. M., B. L. ZHU and R. Z. GUO, 1984, The Change of orientation of stress of the earthquakes before the strong Ninghe earthquake of 1976, *Acta Seismo. Sinica*, **6**, 414-424.

1976年中国寧河地震のシミュレーション解析

地震研究所 袁　一凡
吉沢静代
大沢胖

地震動予測のためには，断層の破壊過程，地震波伝播径路および観測点付近の地盤構造の影響をそれぞれ正しく評価しなければならない．簡単な震源と平行層構造モデルによる短周期地震動の解明は一般に困難であるが，現実に近い震源や構造モデルを用いて，観測記録を検討するというな特定の場合には有効な一つの手法と考えられるので，ここではこの方法を採用することにした．

寧河地震 (M=6.9) は，1976年中国唐山地震の二番目に強い余震である．4ヶ所で観測された加速度記録には，周期約1秒の成分が卓越し，震源に起因するものと予想されるので，これによって，impulse 形の加速度震源関数を仮定している．有限差分法を用いて，特に観測点の地下構造の横方向に不均一な影響を考慮し，観測点にそれぞれ対応する構造モデルを作って，地震動のシミュレーション解析をしてみた．断層のパラメータと破壊様式は計算した加速度波形が観測記録に合うように定めた．記録を cut-off 周波数が 2Hz の low-pass フィルターに通した．計算には計算量と記憶容量を節約するため，くいちがい公式を書き直し，伝達境界に特別処理をするなどいくつかの工夫をした．

結果として，寧河地震は，エネルギーが断層中心付近で解放され，横ずれ成分が大きい．また断層面上で最大加速度は1gを超えるようである．なお，震源の破壊過程がわりあい簡単なことにかかわらず，地震波が特に横方向の不均一な構造の影響を受け，地面での地震動は一層複雑になると思われる．地震動の解明には，その影響を考える必要がある一例といえよう．